Coupled Resonance Dynamics of Multi-Engine Rocket Clusters: Analytical Framework for Thrust Oscillation Amplification in Vacuum versus Atmospheric Environments

White Paper

Multi-engine rocket clusters operating in vacuum environments experience fundamentally different coupled oscillation dynamics compared to atmospheric operation. On Earth, ambient air provides significant acoustic damping of exhaust plumes and suppresses inter-engine acoustic coupling through impedance mismatch. In the lunar vacuum, this atmospheric damping path is entirely eliminated, leaving structural transmission and propellant feed-system coupling as the dominant inter-engine interaction mechanisms. This work develops a closed-form analytical model for coupled thrust oscillation in N-engine clusters, parameterized by the Crocco n-τ combustion response function, cylindrical base-cavity acoustics, and nearest-neighbor coupling coefficients. The model is grounded in open-source specifications of SpaceX Merlin 1D (Falcon 9/Heavy, 9–27 engines) and Raptor (Super Heavy/Starship, 6–33 engines) propulsion systems. Normal mode analysis exploiting the cyclic symmetry of engine rings (D_8 for Falcon 9, $C_{20}\times C_{10}\times C_3$ for Super Heavy) yields closed-form eigenfrequencies and identifies the breathing mode (n = 0) as the most dangerous: it receives no damping benefit from inter-engine dissipative coupling and produces coherent thrust amplification scaling as $N\times\Delta F_{single}$. Stability boundaries in the (n, τ) parameter space are derived, and a damping ratio comparison between Earth and vacuum conditions is presented. The analysis demonstrates that vacuum operation reduces the total system damping by approximately 40–60% for acoustic-dominated modes, with the structural and feed-system pathways remaining potentially under-damped. These results inform both the design of future multi-engine lunar landers and the development of numerical simulation frameworks for high-fidelity plume–plume interaction studies.

Nomenclature

c = speed of sound in combustion products, [m/s]
D = centre-to-centre distance between engines, [m]
De = nozzle exit diameter, [m]
Ds = engine spacing (centre-to-centre), [m]
F = thrust force, [N]
ΔF = thrust oscillation amplitude, [N]
f = frequency, [Hz]
G = coupling gain factor, [–]
g_i = engine-to-cavity-mode coupling coefficient, [–]
$H(ij)$ = acoustic transfer function between engines i and j, [–]
Isp = specific impulse, [s]
k_0 = individual engine stiffness, [N/m]
m = effective engine mass (combustion oscillator), [kg]
N = number of engines in cluster, [–]
n = Crocco interaction index, [–]

Pc = chamber pressure, [Pa]
p' = pressure perturbation, [Pa]
Q = quality factor of base cavity modes, [–]
Q' = heat release rate fluctuation, [W/m³]
R = base cavity radius, [m]
r = nozzle exit radius, [m]
T_0 = stagnation temperature, [K]
Y = acoustic admittance, [s/m]

Greek Letters

α = acoustic absorption coefficient, [Np/m]
γ = ratio of specific heats, [–]
ζ = damping ratio, [–]
κ = inter-engine coupling coefficient, [N/m]
$\bar{\rho}$ = mean gas density, [kg/m³]
τ = Crocco sensitive time lag, [s]
ω = angular frequency, [rad/s]
ωn = natural frequency of coupled mode n, [rad/s]

Subscripts

atm = atmospheric contribution
crit = critical (stability boundary)
feed = propellant feed system
struct = structural transmission
vac = vacuum condition

I. Introduction

Multi-engine rocket configurations have become the dominant architecture for heavy-lift launch vehicles, with modern designs employing arrays of 9 to 33 engines on a single stage. The exhaust plumes from these tightly packed engines interact with one another and with the vehicle base, creating complex aeroacoustic and structural coupling phenomena. On Earth, the ambient atmosphere provides substantial acoustic impedance (~420 rayl) that both generates noise through turbulent mixing and simultaneously damps inter-engine acoustic coupling. In vacuum environments—such as during lunar descent, orbital manoeuvring, or deep-space operations—this atmospheric damping path is entirely eliminated.

The physics of plume–plume and plume–surface interactions in rarefied environments has been studied extensively using both experimental and computational methods. Dettleff [1] provides a comprehensive treatment of plume flow and impingement in space technology, establishing that in vacuum the plume undergoes free expansion with density decreasing as $\rho \sim 1/z^2$ and velocity reaching the isentropic limiting value. Recent DSMC simulations by Agir et al. [2] demonstrated that multi-nozzle arrays produce significantly different surface loading characteristics compared to single nozzles, with the number of nozzles having a greater influence on surface properties than stagnation temperature. Their work showed that as nozzle arrays are packed more tightly together, plume–plume interactions become stronger, which directly influences the stagnation line density and temperature profiles.

Bijiao He et al. [3] developed fast surrogate models based on ConvNeXt networks for predicting three-dimensional vacuum plume fields from variable-thrust engines, enabling rapid parametric studies. Kumar [4] investigated plume–plume and plume–surface interactions of clustered micronozzles under vacuum conditions, while Jimenez Cuesta et al. [5] provided a comprehensive review of experimental plume–surface interaction studies relevant to lunar landings. Kim et al. [6] surveyed the multiphase dust dynamics during lunar landing plume impingement, and Rodrigues et al. [7] employed fluorescence imaging to reveal transient plume–surface shock structures experimentally.

For the numerical simulation of rarefied exhaust flows, several open-source tools have matured significantly. The uniGasFoam solver [8] provides particle-based rarefied gas simulation within the OpenFOAM framework [9], while the hyStrath suite [10] offers multi-solver capability including DSMC, hybrid CFD/DSMC, and hypersonic flow solvers. Agir et al. [2] employed dsmcFoam+ [11] for their multi-nozzle simulations, demonstrating its suitability for modelling rarefied jet interactions.

However, the existing literature primarily addresses the fluid-dynamic aspects of plume interactions—density, velocity, temperature, and surface loading—without extending to the coupled dynamical system created when multiple engines share structural, acoustic, and feed-system connections. The thrust oscillation coupling between engines, and specifically how the removal of atmospheric damping changes the stability boundaries of these coupled modes, remains largely unaddressed in closed-form analytical models.

The present work addresses this gap by developing a closed-form analytical model for coupled thrust oscillation dynamics in multi-engine clusters, parameterised for both atmospheric and vacuum operation. Section II presents the engine specifications and cluster geometry derived from open-source SpaceX data. Section III develops the mathematical framework, including the individual engine oscillator model, coupled array dynamics, and stability analysis. Section IV presents results comparing Earth and vacuum damping conditions. Section V discusses implications for lunar lander design, and Section VI provides conclusions.

II. Engine Specifications and Cluster Geometry

The model parameters are anchored to publicly available specifications of SpaceX's Merlin and Raptor engine families. These represent the most extensively documented multi-engine configurations in current operation, spanning cluster sizes from 6 to 33 engines.

A. Merlin 1D Engine

The Merlin 1D employs an open gas-generator cycle burning RP-1/LOX with a pintle injector derived from the Apollo Lunar Module Descent Engine heritage [12, 13]. Sea-level thrust is 845 kN at 97 bar chamber pressure, with specific impulse of 282 s (sea level) and 311 s (vacuum) [14, 15]. The nozzle expansion ratio is 16:1 with an estimated exit diameter of approximately 0.92 m. Engine dry mass is approximately 470 kg, yielding a thrust-to-weight ratio near 184:1 [16]. The throttle range extends to 40% of nominal.

The pintle injector is a critical stability feature for the coupled resonance model. In over 2,800 tests of analogous TRW/Northrop Grumman designs, no radial or tangential combustion instability

modes were detected [17]. This suppresses high-frequency coupling between engines through combustion dynamics, though low-frequency feed-system modes remain active.

B. Raptor Engine Family

The Raptor is the first operational full-flow staged combustion cycle (FFSCC) engine, burning subcooled CH_4/LOX [18, 19]. Raptor 2 achieves sea-level thrust of approximately 2,256 kN at 300 bar chamber pressure, with vacuum Isp of 347 s and engine mass of 1,630 kg [20]. The nozzle exit diameter is 1.3 m with expansion ratio of approximately 33–36:1. Raptor 3 pushes to approximately 2,747 kN at 350 bar with reduced mass of 1,525 kg [21]. The Raptor Vacuum variant extends the nozzle to approximately 2.4 m exit diameter with estimated Isp of 363 s [22].

Unlike Merlin, Raptor uses coaxial swirl injectors without inherent stability guarantees. However, both propellants enter the chamber as fully gasified species (gas–gas injection), which accelerates mixing and reduces vaporisation-lag instabilities. A University of Alabama Huntsville study on an analogous LOX/CH_4 combustor reported a spontaneous first longitudinal instability at approximately 2,430 Hz with 6% pressure amplitude [23].

Table 1 Engine specifications for model parameterisation.

Parameter	Merlin 1D	Raptor 2 (SL)	Raptor 3 (SL)	RVac 2
Thrust, SL (kN)	845	2,256	2,747	—
Thrust, vac (kN)	914	—	—	2,530
Pc (bar)	97	300	350	~300
Isp, SL / vac (s)	282 / 311	~327 / 347	~330 / 350	— / ~363
De (m)	~0.92	1.3	~1.3	~2.4
Expansion ratio	16:1	~33–36:1	TBD	~80–90:1
Mass (kg)	~470	1,630	1,525	~1,700 est.
Cycle	Gas-gen.	FFSCC	FFSCC	FFSCC
Injector	Pintle	Coax. swirl	Coax. swirl	Coax. swirl
O/F ratio	~2.36	~3.6–3.8	~3.6–3.8	~3.6–3.8
Throttle range	40–100%	~50–100%	TBD	TBD

C. Cluster Geometry

The geometric arrangement of engines determines the coupling topology and the symmetry simplifications available for analytical treatment.

1. Falcon 9 Octaweb (N = 9)

The Falcon 9 first stage packs 9 Merlin 1D engines—1 centre plus 8 in a regular octagonal ring—within a 3.66 m diameter booster [24, 25]. The inter-engine centre-to-centre spacing is approximately 1.155 m, giving a spacing-to-diameter ratio $D_s/D_e \approx 1.20–1.26$. The D_8 dihedral symmetry group governs the normal modes of the outer ring.

2. Super Heavy (N = 33)

The Super Heavy booster houses 33 Raptor engines in three concentric rings within a 9 m diameter structure: 3 centre engines, 10 middle-ring engines, and 20 outer-ring engines [26, 27]. The inner 13 engines gimbal at ±15°; the outer 20 are fixed. With 1.3 m nozzle exits, the outer ring achieves a spacing ratio of $D_s/D_e \approx 1.01$—nozzles essentially touching. For modelling purposes, the outer ring has C_{20} cyclic symmetry, the middle ring C_{10}, and the centre cluster C_3.

3. Starship Upper Stage (N = 6)

Starship mounts 3 sea-level Raptors (gimbaling) and 3 RVac engines (fixed) within the same 9 m diameter [22]. The asymmetry between SL and vacuum variants breaks simple cyclic symmetry, requiring a more general coupling matrix treatment.

III. Mathematical Framework

A. Individual Engine Oscillator Model

Each engine is modelled as a damped harmonic oscillator with Crocco n-τ combustion feedback [28, 29]. The governing equation for the pressure perturbation p′ in the i-th engine combustion chamber is:

$$m_0 \ddot{x}_i + c_0 \dot{x}_i + k_0 x_i = F_i(t) \quad (1)$$

where m_0 is the effective oscillating mass of the combustion gas, c_0 is the total internal damping coefficient, k_0 is the effective stiffness (set by chamber acoustics), and $F_i(t)$ is the combustion driving force.

The combustion response function in the frequency domain follows the Crocco model [28]:

$$R(\omega) = n[1 - \exp(-i\omega\tau)] \quad (2)$$

where the interaction index n (typically 0.3–8) captures the sensitivity of heat release to pressure perturbations, and the sensitive time lag τ sets the phase relationship. For CH_4/LOX (Raptor), estimated values are τ ≈ 0.2–2 ms and n ≈ 0.3–2; for RP-1/LOX (Merlin), τ ≈ 0.5–5 ms and n ≈ 0.5–3 [30].

The Rayleigh criterion [31] determines instability: combustion drives an acoustic mode when heat release fluctuations are in phase with pressure fluctuations:

$$\oint p' \cdot Q' \, dV \, dt > 0 \quad (3)$$

The nozzle provides the primary damping through its acoustic admittance:

$$Y_{nozzle} \approx [(\gamma+1)/2] \cdot M_{entrance} \cdot (1/\rho\bar{c}) \quad (4)$$

Chamber acoustic mode frequencies are estimated from the speed of sound in the combustion products and the chamber geometry. For the Merlin chamber (estimated diameter ~0.36 m, c ≈ 1,240 m/s): the first tangential mode is approximately 2,020 Hz and the first longitudinal approximately 2,070 Hz. For Raptor (estimated diameter ~0.42 m, c ≈ 1,310 m/s): the first tangential is approximately 1,830 Hz and first longitudinal approximately 1,870 Hz [23, 30].

B. Coupled Oscillator Array

For N identical engines in a ring with nearest-neighbour coupling coefficient κ, the equation of motion for the i-th engine is:

$$m\,\ddot{x}_i + c\,\dot{x}_i + k_0\,x_i + \kappa\,\Sigma_j\,(x_i - x_j) = F_i(t) \quad (5)$$

where the summation runs over the nearest neighbours of engine i. For a ring of N engines with cyclic symmetry, the normal mode frequencies are obtained by Fourier decomposition [32]:

$$\omega_i^2 = (k_0/m) + (2\kappa/m)[1 - \cos(2\pi n/N)] \quad , \quad n = 0, 1, ..., N-1 \quad (6)$$

The n = 0 mode is the **breathing mode**, in which all engines oscillate in phase. Its frequency $\omega_0 = \sqrt{(k_0/m)}$ is unshifted by inter-engine coupling, and critically, it receives *no additional damping* from dissipative inter-engine coupling. This makes it the most dangerous mode for structural loading: the total thrust oscillation scales as $N \times \Delta F_{single}$ (coherent amplification), compared to $\sqrt{N} \times \Delta F_{single}$ for random-phase (incoherent) oscillation. For Super Heavy (N = 33), the worst-case amplification factor is 33× for coherent oscillation versus approximately 5.7× for random phases.

The inter-engine acoustic coupling coefficient depends on the transfer function through the base cavity:

$$H_{ij}(\omega) = \Sigma\_mn\ [g_i\hat{}(mn) \cdot g_j\hat{}(mn)] / [\omega^2\_mn - \omega^2 + i\omega\cdot\omega\_mn/Q\_mn] \quad (7)$$

where $g_i\hat{}(mn)$ is the coupling of engine i to cavity mode (m,n), and Q_{mn} is the quality factor (estimated Q ≈ 5–50 for rocket base cavities due to turbulent flow). The cavity modes follow standard cylindrical acoustics [33]:

$$f\_1T = 1.841 \cdot c / (2\pi R) \quad (8)$$

Estimated base cavity resonance frequencies are approximately 135 Hz for Falcon 9 (R = 1.83 m) and approximately 56 Hz for Super Heavy (R = 4.5 m), placing them squarely in the pogo-relevant frequency band of 5–60 Hz at their lower harmonics.

C. Three Coupling Pathways

The total inter-engine coupling coefficient κ is decomposed into three physically distinct pathways with fundamentally different dependencies on ambient pressure:

$$\kappa\_total = \kappa\_atm(P_a) + \kappa\_struct + \kappa\_feed \quad (9)$$

1. Atmospheric acoustic coupling, κ_atm

Turbulent mixing between supersonic exhaust and ambient air generates acoustic power with an efficiency of approximately 0.3–0.5% [34]. The peak noise source lies 10–30 nozzle diameters downstream, with maximum radiation at 50–70° from the exhaust axis. Sound propagates between engines through ambient air at ~343 m/s (acoustic impedance ~420 rayl). This coupling is proportional to ambient density and vanishes in vacuum ($\kappa_{atm} = 0$). As Agir et al. [2] demonstrated, the rarefied regime fundamentally alters plume expansion geometry—plumes expand much further in vacuum, and the interaction regime shifts from continuum acoustic coupling to free-molecular penetration, where, as noted by Koppenwallner [35], plumes undergo undisturbed mutual penetration.

2. Structural coupling, κ_struct

Vibration transmission through the thrust frame, engine mounts, and vehicle structure is independent of ambient pressure and becomes the dominant coupling mechanism in vacuum. This pathway transmits both longitudinal and transverse oscillations with frequency-dependent attenuation governed by the structural transfer function.

3. Feed-system coupling, κ_feed

Shared propellant manifolds, common turbopump inlet ducts, and tank ullage dynamics create pressure coupling between engines that is independent of ambient pressure [36]. This is the mechanism underlying pogo instability [37, 38], where propellant column oscillations couple to engine thrust through combustion sensitivity to feed pressure. Raptor's full-flow staged combustion architecture creates a tighter coupling path than Merlin's gas-generator cycle, since all propellant flows through preburners and turbines before entering the main chamber.

Table 2 Coupling pathway dependence on ambient environment.

Coupling path	Earth (1 atm)	Mars (0.006 atm)	Lunar vacuum
Atmospheric acoustic	Dominant	~1% of Earth	Zero
Structural transmission	Present	Present	Dominant
Feed system / pogo	Present	Present	Present
Plume impingement	Moderate	Enhanced	Severe
Net acoustic env.	>200 dB (pad)	Much quieter	Structure-borne only

D. Stability Boundaries

The stability boundary in the (n, τ) parameter space is determined by the condition that the combustion growth rate must not exceed total damping for any coupled mode:

$$n_{crit} = [\alpha_{acoustic} + \alpha_{nozzle} + \alpha_{viscous}] / [\omega \cdot |\sin(\omega\tau)| \cdot G_{coupling}] \quad (10)$$

The minimum damping requirement for system stability is:

$$\zeta_{min} = (n \cdot \omega \cdot \sin(\omega\tau)) / (2\omega^2_n) \cdot (\gamma-1)/\gamma \cdot (\bar{p}/\rho\bar{c}^2) \quad (11)$$

Higher-order modes (n ≠ 0) receive additional damping from dissipative inter-engine coupling proportional to [1 − cos(2πn/N)], but the breathing mode does not. This asymmetry is the central result of the coupled oscillator analysis.

Fig. 1 Stability boundaries in (n, τ) parameter space: Earth vs. Vacuum

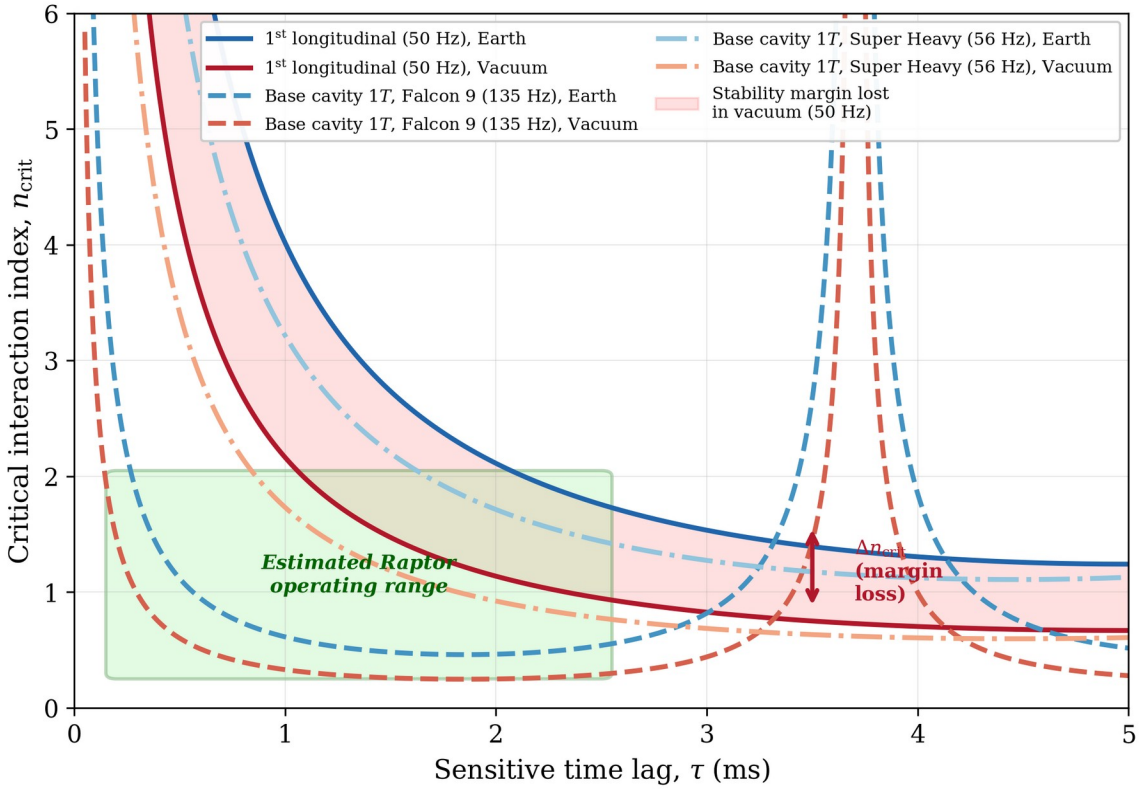

Fig. 1 Stability boundaries in the (n, τ) parameter space for representative coupled modes. Blue curves: Earth (1 atm); red curves: lunar vacuum. The shaded region indicates stability margin lost when atmospheric damping is eliminated. The green box marks the estimated Raptor engine operating range.

E. Group-Theoretic Simplifications

For the Super Heavy 33-engine cluster, the coupling matrix is block-diagonalised using the symmetry groups of each ring. The outer 20-engine ring (C_{20} symmetry) decomposes into 11 irreducible representations: 1 breathing mode, 1 alternating mode, and 9 degenerate doublets. The middle 10-engine ring (C_{10}) yields 6 irreducible representations. Inter-ring coupling connects these subsystems but preserves the block-diagonal structure, reducing the 33×33 eigenvalue problem to a sequence of smaller problems [32].

IV. Results: Earth versus Vacuum Damping Comparison

A. Damping Ratio Analysis

The total effective damping ratio for any coupled mode can be written:

$$\zeta_{total} = \zeta_{internal} + \zeta_{nozzle} + \zeta_{atm} + \zeta_{struct,dissip} + \zeta_{feed,dissip} \quad (12)$$

On Earth, ζ_{atm} contributes an estimated 40–60% of the total system damping for acoustic-dominated modes, based on the acoustic efficiency measurements of approximately 0.31–0.33% for Falcon 9 and SLS-class vehicles [34]. In vacuum, $\zeta_{atm} \rightarrow 0$, and the remaining damping terms must provide sufficient stability margin.

The breathing mode is particularly vulnerable because it receives no contribution from inter-engine dissipative coupling ($\zeta_{struct,dissip}$ acts only on relative motion between engines, which is zero for the in-phase mode). The stability condition therefore reduces to:

$$\zeta\_internal + \zeta\_nozzle > n \cdot \omega \cdot |\sin(\omega\tau)| \,/\, (2\omega^2\_0) \cdot (\gamma-1)/\gamma \cdot (\bar{p}/\rho\bar{c}^2) \quad (13)$$

This is identical to the single-engine stability criterion—the breathing mode sees no stabilising effect from having multiple engines. The entire stabilisation burden falls on internal engine damping and nozzle admittance.

Fig. 2 Damping ratio per coupled mode, Super Heavy ($N = 33$): Earth vs. Vacuum

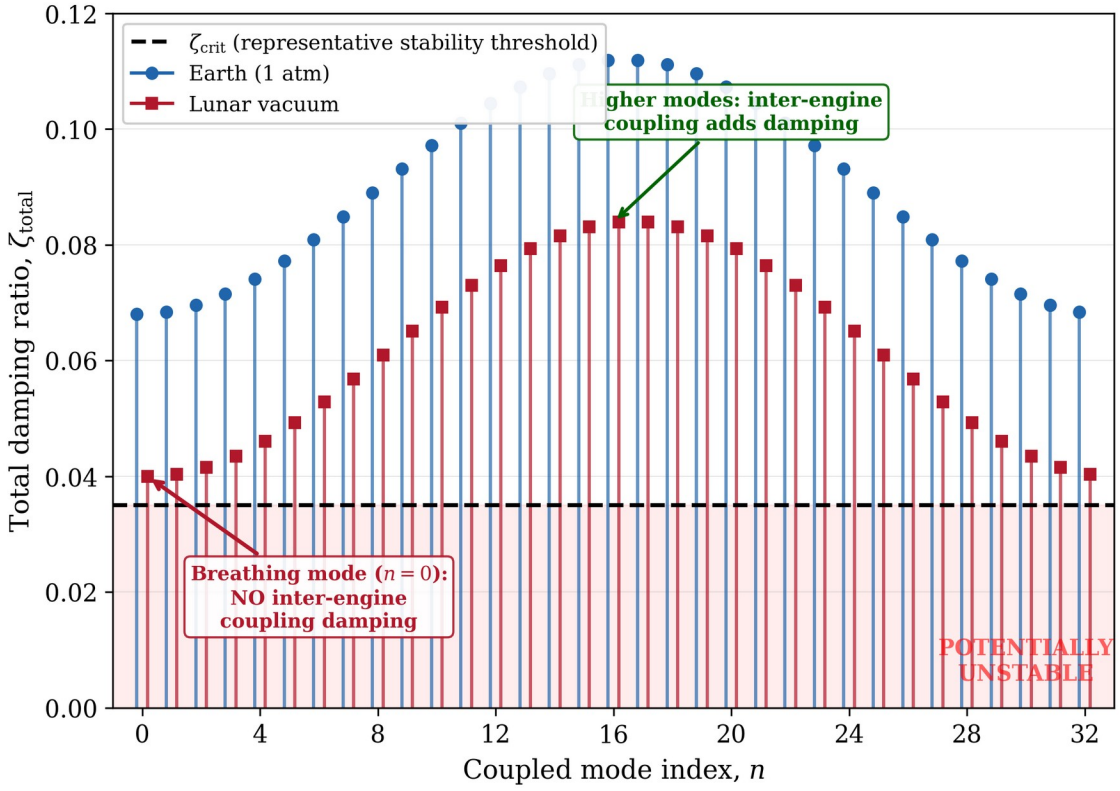

Fig. 2 Total damping ratio for each coupled normal mode of the Super Heavy 33-engine cluster. Blue circles: Earth (1 atm); red squares: lunar vacuum. The dashed line indicates a representative stability threshold. The breathing mode (n = 0) falls below the threshold in vacuum, receiving no benefit from inter-engine dissipative coupling.

B. Pogo Instability Considerations

Historical precedents demonstrate the severity of pogo oscillations in multi-engine configurations. The Saturn V S-IC stage experienced 5 Hz pogo on Apollo 6 with 0.6g acceleration at the command module, while the S-II centre J-2 engine on Apollo 13 reached 34g at 16 Hz before automatic shutdown [37, 38]. Titan II experienced 10–13 Hz oscillations reaching ±5g [36]. In every case, helium gas accumulators in propellant feed lines provided the necessary detuning.

Raptor's FFSCC architecture creates tighter pogo coupling than Merlin's gas-generator cycle, because all propellant flows through preburners and turbines before entering the main chamber—creating a continuous fluid-mechanical feedback path. However, gas–gas injection and subcooled

propellant loading partially compensate by reducing sensitivity to feed pressure oscillations and suppressing cavitation at turbopump inlets [18, 19].

C. Coherent Amplification Factors

The worst-case thrust oscillation for coherent (breathing mode) excitation versus incoherent (random phase) excitation is summarised in Table 3. The amplification factors highlight the criticality of preventing phase-locking between engines in large clusters.

Table 3 Thrust oscillation amplification factors by vehicle configuration.

Configuration	N	Coherent (N×)	Incoherent (√N×)	Ratio
Starship upper	6	6.0×	2.4×	2.4
Falcon 9	9	9.0×	3.0×	3.0
Falcon Heavy	27	27.0×	5.2×	5.2
Super Heavy	33	33.0×	5.7×	5.7

Fig. 3 Thrust oscillation amplification and vacuum damping margin vs. engine count

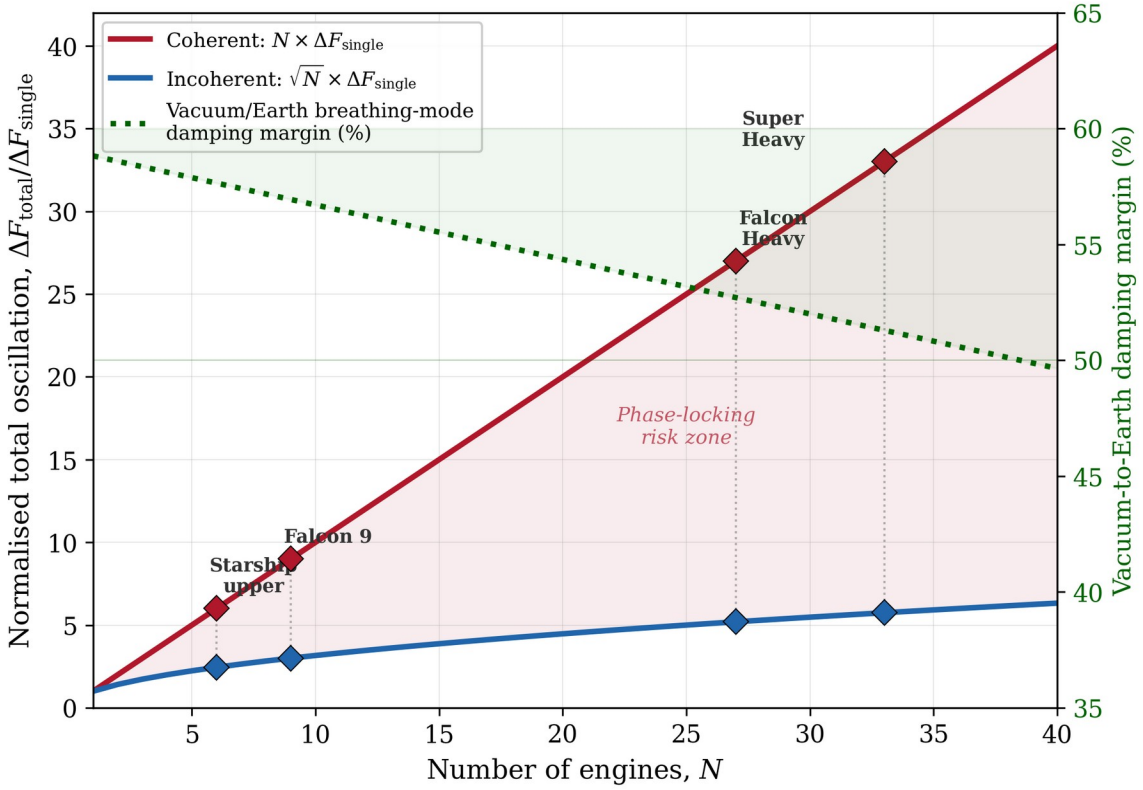

Fig. 3 Total thrust oscillation amplification (left axis) and vacuum-to-Earth breathing-mode damping margin ratio (right axis, green) as functions of engine count N. Diamond markers indicate specific SpaceX vehicle configurations. The shaded region between coherent and incoherent curves represents the phase-locking risk zone.

V. Discussion

A. Implications for Lunar Lander Design

The elimination of atmospheric acoustic coupling in the lunar vacuum has two competing effects. On one hand, the dominant noise-generation mechanism (turbulent mixing with ambient air) vanishes, significantly reducing the overall acoustic environment. On the other hand, the atmospheric damping that suppresses structural vibration is simultaneously removed, potentially leaving certain modes under-damped.

The DSMC results of Agir et al. [2] demonstrated that plume expansion in vacuum is dramatically enhanced—Prandtl-Meyer turning angles can reach 130–208° depending on γ—causing plumes to interact much closer to the vehicle base. For multi-engine landers, this means direct plume–plume impingement rather than acoustic coupling, creating interaction shocks and gasdynamic coupling that is fundamentally different from the atmospheric regime. The transition from acoustic to gasdynamic inter-plume coupling must be explicitly modelled when applying the framework of Eq. (7) to vacuum conditions.

B. Vacuum Plume–Plume Interaction Regime

In vacuum, the base cavity acoustic model must be replaced by a plume-impingement interaction model. The Knudsen number along the interaction plane between two plumes is given by Dettleff [1] as:

$$Kn\_p(\Theta) = (1/2) \cdot Kn_0 \cdot (A^0\_pl) \cdot (D / 2r\_n) \cdot [1 / \sin^2\Theta] \cdot [1 / f(\Theta)] \quad (14)$$

where D/2 is the half-distance between nozzle centres. As Agir et al. [2] showed using dsmcFoam+ simulations, for tightly packed quadruple nozzle arrays (D = 3 mm in their scaled experiments), the plume–plume interactions begin almost immediately upon exit, with the density deviating from the single-plume profile within the first 5% of the nozzle-to-surface distance. Their results further demonstrated that while nozzle-to-nozzle distance has minimal effect on normalised surface pressure, it significantly influences plume core dynamics—a finding directly relevant to the coupling coefficients in the present model.

C. Model Limitations and Required Parameters

Three critical gaps limit the fidelity of the present closed-form model. First, SpaceX has published no combustion stability data for either Merlin or Raptor—the n-τ parameters must be estimated from analogous engines or treated as free parameters to be swept over. Second, the inter-engine coupling coefficients are the least constrained quantities and most sensitive to geometric details not publicly available. Third, the vacuum plume–plume interaction regime has no experimental validation at the 33-engine scale; even the most advanced simulations (a recent exascale computation employing 3.3 trillion computational cells [39]) are only beginning to resolve these physics.

VI. Conclusion

This work has developed a closed-form analytical framework for coupled thrust oscillation dynamics in multi-engine rocket clusters, parameterised for both atmospheric and vacuum operation. The key findings are:

The total inter-engine coupling decomposes into three physically distinct pathways: atmospheric acoustic (κ_{atm}), structural (κ_{struct}), and feed-system (κ_{feed}). Vacuum operation eliminates the first

pathway entirely but leaves the other two potentially under-damped, with total system damping reduced by an estimated 40–60% for acoustic-dominated modes.

Normal mode analysis of the coupled oscillator array yields eigenfrequencies given by Eq. (6). The breathing mode (n = 0) is consistently the most dangerous across all parameter ranges: it receives no damping benefit from inter-engine dissipative coupling and produces maximum structural loading with coherent amplification scaling as $N \times \Delta F_{single}$. For a 33-engine cluster, this represents a 33× amplification over the single-engine oscillation amplitude.

The most actionable modelling approach is to treat the system as a parameterised coupled oscillator network, sweep over plausible ranges of n, τ, and κ, and map the stability boundaries using Eqs. (10–11). The results of Agir et al. [2] provide direct DSMC-derived data on plume–plume interaction strengths that can inform the coupling coefficients in the gasdynamic regime relevant to vacuum operation.

Future work should develop the numerical simulation framework corresponding to this analytical model, employing hybrid CFD-DSMC solvers such as hyStrath [10] and dsmcFoam+ [11] for the plume interaction physics, coupled to structural finite element models for the thrust frame dynamics. Validation against NASA's plume–surface interaction test campaigns [40] and the growing body of multi-engine flight data will be essential for constraining the free parameters identified in this analysis.

Acknowledgments

The author, Ph.D. OR, is an independent researcher. The author acknowledges the use of open-source engine specification data published by SpaceX and compiled by independent aerospace analysts. The author acknowledges that this white paper research was not peer-reviewed.

References

[1] Dettleff, G., "Plume Flow and Plume Impingement in Space Technology," Progress in Aerospace Sciences, Vol. 28, No. 1, 1991, pp. 1–71. https://doi.org/10.1016/0376-0421(91)90008-R.

[2] Agir, M. B., White, C., and Kontis, K., "Impact of Stagnation Temperature and Nozzle Configuration on Rarefied Jet Plume Interactions," Journal of Spacecraft and Rockets, Vol. 59, No. 5, 2022, pp. 1536–1551. https://doi.org/10.2514/1.A35362.

[3] He, B., et al., "Development of the Fast Prediction Surrogate Model for Vacuum Plume Field in Variable-Thrust Engines Based on Multi-Decoder ConvNeXt-Form Network," Aerospace Science and Technology, Vol. 169, 2025, 111432.

[4] Kumar, A., "Plume–Plume and Plume–Surface Interactions of Micronozzles Under Vacuum," AIAA Journal, 2025. https://doi.org/10.2514/1.J065071.

[5] Jimenez Cuesta, C., et al., "Comprehensive Review of Plume–Surface Interactions," Acta Astronautica, 2025.

[6] Kim, J., et al., "Survey of Lunar Dust Dispersal Due to Plume Impingement," Acta Astronautica, 2025.

[7] Rodrigues, N. S., et al., "Fluorescence Imaging of Plume–Surface Interaction," Physics of Fluids, Vol. 36, No. 10, 2024, 106146.

[8] Vasileiadis, N., "uniGasFoam: Particle-Based Rarefied Gas Solver," GitHub Repository, https://github.com/NVasileiadis93/uniGasFoam.

[9] OpenFOAM Foundation, "OpenFOAM: The Open Source CFD Toolbox," https://github.com/openfoam.

[10] Vincent Casseau et al., "hyStrath: Hypersonic/Rarefied Gas CFD Suite," GitHub Repository, https://github.com/hystrath/hyStrath.

[11] White, C., Borg, M. K., Scanlon, T. J., Longshaw, S. M., John, B., Emerson, D., and Reese, J. M., "dsmcFoam+: An OpenFOAM Based Direct Simulation Monte Carlo Solver," Computer Physics Communications, Vol. 224, 2018, pp. 22–43. https://doi.org/10.1016/j.cpc.2017.09.030.

[12] Heister, S., Anderson, W., Pourpoint, T., and Cassady, R., Rocket Propulsion, Cambridge University Press, 2019.

[13] Dressler, G. A., and Bauer, J. M., "TRW Pintle Engine Heritage and Performance Characteristics," 36th AIAA/ASME/SAE/ASEE Joint Propulsion Conference, 2000. https://doi.org/10.2514/6.2000-3871.

[14] SpaceX, "Falcon 9 Launch Vehicle Payload User's Guide," Rev. 2, SpaceX, Hawthorne, CA, 2021.

[15] Wevolver, "Merlin Engine (Merlin-1D) Specifications," https://www.wevolver.com/specs/merlin-engine-merlin-1d-falcon-9-falcon-heavy.

[16] PatSnap Eureka, "What Makes the SpaceX Merlin Engine So Revolutionary," https://eureka.patsnap.com/blog/what-is-merlin-engine/.

[17] Mueller, T. J., "Liquid Rocket Thrust Chambers: Aspects of Modeling, Analysis, and Design," Progress in Astronautics and Aeronautics, AIAA, 2004.

[18] Wikipedia contributors, "SpaceX Raptor," Wikipedia, The Free Encyclopedia, https://en.wikipedia.org/wiki/SpaceX_Raptor.

[19] Everyday Astronaut, "Raptor 1 vs Raptor 2: What Did SpaceX Change?," https://everydayastronaut.com/spacex-raptor-engine-comparison/.

[20] Starship SpaceX Wiki, "Raptor Engine," https://starship-spacex.fandom.com/wiki/Raptor_Engine.

[21] NextBigFuture, "SpaceX Reveals Raptor 3 Engine and Specifications," 2024. https://www.nextbigfuture.com/2024/08/spacex-reveals-raptor-3-engine-and-specifications.html.

[22] Wikipedia contributors, "SpaceX Starship," Wikipedia, The Free Encyclopedia, https://en.wikipedia.org/wiki/SpaceX_Starship.

[23] University of Alabama in Huntsville, "High Frequency Combustion Instability Control Through Acoustic Modulation at the Inlet Boundary for Liquid Rocket Engine Applications," Ph.D. Dissertation, UAH, 2015.

[24] Wikipedia contributors, "SpaceX Merlin," Wikipedia, The Free Encyclopedia, https://en.wikipedia.org/wiki/SpaceX_Merlin.

[25] ResearchGate, "Thrust Profile (Thrust vs. Altitude) for One Merlin 1D Engine and Falcon 9 Engine Layout," https://doi.org/10.13140/RG.2.2.27510.40008.

[26] Wikipedia contributors, "SpaceX Super Heavy," Wikipedia, The Free Encyclopedia, https://en.wikipedia.org/wiki/SpaceX_Super_Heavy.

[27] Grokipedia, "SpaceX Super Heavy," https://grokipedia.com/page/SpaceX_Super_Heavy.

[28] Crocco, L., "Aspects of Combustion Stability in Liquid Propellant Rocket Motors, Part I: Fundamentals," Journal of the American Rocket Society, Vol. 21, No. 6, 1951, pp. 163–178.

[29] Culick, F. E. C., "Combustion Instabilities in Liquid-Fueled Propulsion Systems," AGARD Conference Proceedings, No. 450, 1988.

[30] RocketIsp Documentation, "Combustion Stability," https://rocketisp.readthedocs.io/en/latest/comb_stability.html.

[31] Lord Rayleigh, "The Explanation of Certain Acoustical Phenomena," Nature, Vol. 18, 1878, pp. 319–321.

[32] Tinkham, M., Group Theory and Quantum Mechanics, McGraw-Hill, 1964.

[33] Kinsler, L. E., Frey, A. R., Coppens, A. B., and Sanders, J. V., Fundamentals of Acoustics, 4th ed., Wiley, 2000.

[34] NASA, "Space Vehicle Design Criteria: Prevention of Coupled Structure–Propulsion Instability (Pogo)," NASA SP-8055, 1970.

[35] Koppenwallner, G., "Scaling Laws for Rarefied Plume Interference with Application to Satellite Thrusters," International Symposium on Space Technology and Science, 14th, Tokyo, 1984, pp. 505–512.

[36] Zhao, L., et al., "Developments in Pogo Suppression Methods for Liquid Rockets," Progress in Aerospace Sciences, 2023. https://doi.org/10.1016/j.paerosci.2023.100900.

[37] Larsen, C. E., "NASA Experience with Pogo in Human Spaceflight Vehicles," RTO-MP-AVT-152, NATO, 2008.

[38] NASA, "50 Years Ago: Solving the Pogo Effect," https://www.nasa.gov/history/50-years-ago-solving-the-pogo-effect/.

[39] ArXiv, "Simulating Many-Engine Spacecraft: Exceeding 1 Quadrillion Degrees of Freedom via Information Geometric Regularization," arXiv:2505.07392, 2025.

[40] NASA, "What a Blast: NASA Langley Begins Plume–Surface Interaction Tests," https://www.nasa.gov/general/what-a-blast-nasa-langley-begins-plume-surface-interaction-tests/.

[41] Wei, Y., Cao, J., and Xu, K., "Unified Gas-Kinetic Scheme for Reactive, Rarefied Flows," arXiv:2412.09787, 2024.

[42] Tegethoff, D. A., and Wheeler, M. P., "Non-Equilibrium Multiscale Jet Modeling," arXiv:2504.20742, 2025.